Nebular Line Emission During the Epoch of Reionization

Stephen M. Wilkins,[1]* Ciaran Fairhurst,[1] Christopher C. Lovell,[1] Jussi Kuusisto,[1] Aswin P. Vijayan,[1] Yu Feng,[2,3] Tiziana Di Matteo,[2] Rupert Croft,[2]

[1] *Astronomy Centre, Department of Physics and Astronomy, University of Sussex, Brighton, BN1 9QH, UK*

[2] *McWilliams Center for Cosmology, Carnegie Mellon University, Pittsburgh PA, 15213, USA*

[3] *Berkeley Center for Cosmological Physics, University of California, Berkeley, Berkeley CA, 94720, USA*

ABSTRACT

Nebular emission lines associated with galactic H II regions carry information about both physical properties of the ionised gas and the source of ionising photons as well as providing the opportunity of measuring accurate redshifts and thus distances once a cosmological model is assumed. While nebular line emission has been extensively studied at lower redshift there are currently only few constraints within the epoch of reionisation (EoR, $z > 6$), chiefly due to the lack of sensitive near-IR spectrographs. However, this will soon change with the arrival of the *Webb Telescope* providing sensitive near-IR spectroscopy covering the rest-frame UV and optical emission of galaxies in the EoR. In anticipation of *Webb* we combine the large cosmological hydrodynamical simulation BlueTides with photoionisation modelling to predict the nebular emission line properties of galaxies at $z = 8 \to 13$. One key result is that the predicted ratio of the Hα recombination line luminosity to the star formation rate differs significantly from commonly assumed calibrations.

Key words: galaxies: high-redshift – galaxies: photometry – methods: numerical – galaxies: luminosity function, mass function

1 INTRODUCTION

Massive stars and active galactic nuclei (AGN) are often intense sources of Lyman-continuum (LyC, or hydrogen ionising) photons resulting in the formation of regions of ionised gas in their surroundings (e.g. H II regions). The emission from these regions carries information about the physical conditions in the interstellar medium (ISM) as well as the source of the ionising photons themselves. Key properties that can be constrained include the star formation rate (e.g. Kennicutt & Evans 2012), gas metallicity (e.g. Tremonti et al. 2004), temperature, and density, dust content (e.g. Reddy et al. 2015), and the presence of an AGN (e.g. Baldwin et al. 1981). Nebular line emission enables the accurate measurement of redshifts, and thus distances once a cosmological model is assumed.

While there has been extensive progress in obserserving line emission at low (e.g. Brinchmann et al. 2004) and intermediate (e.g. Steidel et al. 1996; Shapley et al. 2003) redshifts there are few direct constraints at high-redshift. This

is predominantly due to lack of sensitive near-IR spectrographs, particularly at $> 2\mu$m where the rest-frame optical lines lie at $z > 4$, and the comparative lack of strong lines, other than Lyman-α, in the rest-frame UV.

The small number of detections at high-redshift come overwhelmingly from Lyman-α (e.g. Stark et al. 2010; Pentericci et al. 2011; Stark et al. 2011; Caruana et al. 2012; Stark et al. 2013; Finkelstein et al. 2013; Caruana et al. 2014; Stark et al. 2017) though there has now been a handful of detections of the [C IV]λ1548 and [C III],C III]λ1907, 1090 lines (Stark et al. 2015a,b, 2017).

The presence of extremely strong optical lines can also be indirectly inferred from their impact on broadband photometry (e.g. Schaerer & de Barros 2010; Stark et al. 2013; Wilkins et al. 2013; Smit et al. 2014; Wilkins et al. 2016a; de-Barros 2019) yielding constraints now available up to $z \approx 8$ (deBarros 2019).

While existing observational constraints in the EoR are limited this will soon change with the arrival of the *Webb Telescope*. *Webb*'s NIRSpec instrument will provide deep near-IR single slit, multi-object, and integral field spectroscopy from $\sim 0.7 - 5\mu$m, while the NIRISS and NIRCam

* E-mail: s.wilkins@sussex.ac.uk

instruments will, together, provide wide field slitless spectroscopy over a similar range. This is sufficient to encompass all the strong optical lines to $z \sim 7$ with [OII] potentially accessible to $z \sim 12$. *Webb*'s mid-infrared instrument (MIRI) will provide mid-IR single slit, and slitless spectroscopy at $\lambda > 5\mu m$, albeit at much lower sensitivity and thus will likely only detect line emission for the brightest sources in the EoR.

The existing direct and indirect constraints and the nearing prospect of *Webb* motivates us to produce predictions for the nebular emission line properties of galaxies in the EoR. In this paper, we combine the large BLUETIDES hydrodynamical simulation with photoionisation modelling to predict the nebular line properties of galaxies in the EoR, specifically ($z = 8 \rightarrow 13$). As part of this paper we also explore some of the photon-ionisation modelling assumptions including the choice stellar population synthesis (SPS) model and initial mass function (IMF). Prior to *Webb* these predictions can be used to optimise the design of surveys targeting emission line in the EoR. Ultimately, however the, observation of these lines will provide a powerful constraint on the physics incorporated into galaxy formation models.

This paper is structured as follows: in Section 2 we describe the BLUETIDES simulation and our methodology for calculating the nebular emission line properties. In Section 3 we present our predictions, including examining the effect of the choice of initial mass function and stellar population synthesis model (§3.3) and providing a comparison with existing observational constraints (§3.4). In Section 4 we present our conclusions. In Appendix A we briefly present an overview of the production of ionising photons by stellar populations and photoionisation modelling.

By default we make the following modelling choices: we assume the BPASS v2.2.1 SPS model () and a Chabrier (2003) IMF.

2 MODELLING NEBULAR EMISSION IN BLUETIDES

2.1 The BlueTides Simulation

The BLUETIDES simulation (http://bluetides-project.org/, see Feng et al. 2015, 2016, for description of the simulation physics) is an extremely large galaxy formation simulation designed to study the early phase of galaxy formation and evolution with a specific focus on the formation of the massive galaxies. BLUETIDES phase 1 evolved a $(400/h \approx 577)^3$ cMpc^3 cube to $z = 8$ using 2×7040^3 particles assuming the cosmological parameters from the *Wilkinson Microwave Anisotropy Probe* nine year data release (Hinshaw et al. 2013). The properties of galaxies in the simulation are extensively described in Feng et al. (2015, 2016); Wilkins et al. (2016b,a); Waters et al. (2016a,b); Di Matteo et al. (2016); Wilkins et al. (2017); **?**.

2.1.1 *Ages and Metallicities of Galaxies in BLUETIDES*

As emission line luminosities and equivalent widths are predominantly driven by galaxy star formation and metal enrichment histories it is useful to explore the average ages

and metallicities predicted by BLUETIDES. The mean stellar age and mean metallicity of young ($< 10\,\mathrm{Myr}$) stars are shown as a function of stellar mass for a range of redshifts in Figure 1. These correlations were previously discussed in more detail in Wilkins et al. (2017) while a more detailed of analysis of the joint star formation and metal enrichment history is presented in Fairhurst et al. *in-prep*. In short the mean stellar age appears to show little dependence on mass but evolves strongly with redshift while the mean metallicity of young stars shows a power-law dependence ($Z \propto M^{0.4}$) on stellar mass but little evolution with redshift.

2.2 Nebular Emission Modelling

To model the nebular emission from entire galaxies we start by associating each star particle with an intrinsic stellar spectral energy distribution (SED) based on its age and metallicity. Using this SED we then calculate the corresponding nebular emission using the 2017 (C17.01) version of the popular CLOUDY code (Ferland et al. 2017)[1]. Additional details on our photoionisation modelling are given in Appendix A. The resulting *intrinsic* nebular emission associated with each galaxy is then simply the sum over all the star particles.

2.2.1 *Star Formation History Sampling Effects*

The LyC production rate is a very strong function of the age, and to a lesser extent, metallicity of the stellar population (see §A1). As the star formation history of each galaxy is potentially sampled by (at the lowest stellar masses considered) a small (~ 100) number of individual star particles, this raises the possibility that the predicted line properties differs from the truth because of SFH sampling affects. To explore the potential extent of this effect we re-sample the average star formation history of galaxies at $z = 8$ using different numbers of particles ($n = 10^2 - 10^4$) corresponding roughly to stellar masses of $10^8 - 10^{10}\,\mathrm{M_\odot}$. The result of this analysis is shown in Fig. 2. This test reveals that there is no significant bias in the average (median or mean) of the predicted line luminosity (in this case Hα), even at low-masses. However, at low-masses there is considerable scatter (≈ 0.1 dex for $n = 300$ particles / $M_\star \approx 2.5 \times 10^8\,\mathrm{M_\odot}$). This type of scatter could potentially flatten the predicted luminosity function at low-luminosities.

2.3 Modelling attenuation by dust

Dust attenuation in BLUETIDES is modelled using a simple scheme which links the smoothed metal density integrated along lines of sight to each star particle within each galaxy to the dust optical depth in the V-band (550 nm). Attenuation at other wavelengths is determined using a simple attenuation curve of the of the form,

$$\tau_\lambda = \tau_V \times (\lambda/550\mathrm{nm})^{-1}. \tag{1}$$

This model has a single free parameter which effectively links the surface density of metals to the optical depth. This parameter is tuned to recover the shape of the of the observed
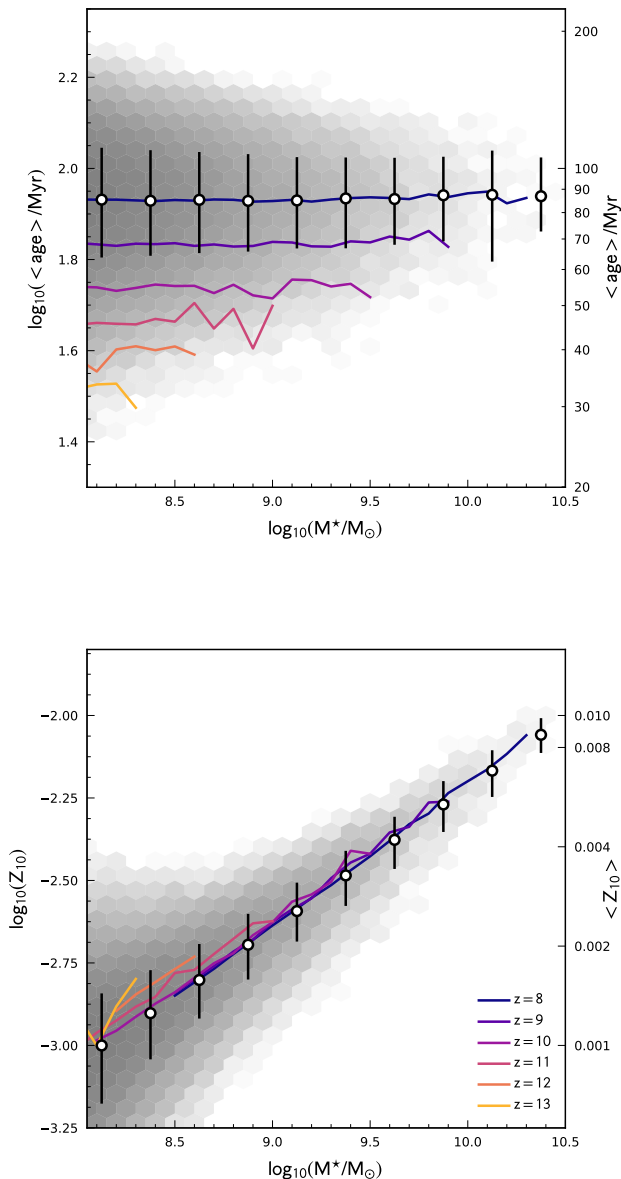
---

[1] https://www.nublado.org

Figure 2. The ratio of the modelled line luminosity compared to the true luminosity as a function of the number of particles used to sample the star formation history.

widths unaffected[2]. In reality it is likely that at least some fraction of ionising photons are absorbed by dust prior to being reprocessed.

3 PREDICTIONS FOR BLUETIDES

Using the methodology outlined, we calculate the luminosity and EWs of twelve UV and optical lines for all galaxies in BLUETIDES from $z = 13 \rightarrow 8$ with $M_\star > 10^8$ M$_\odot$. This encompasses over 200,000 galaxies in total with $\approx$150,000 at $z = 8$ and 126 at $z = 13$.

3.1 Line Luminosities and Equivalent Width Distributions

Predictions for the line luminosities and EWs and their dependence with stellar mass and UV luminosity are summarised, for 6 prominent lines, in Fig. 3. These predictions assume the BPASS v2.2.1 SPS model and a modified Salpeter IMF. In Appendix B we also provide more detailed plots for each individual line or doublet. Tabulated results for all twelve lines are also all available in electronic form here.

In summary, the luminosity function of each line broadly follows a similar trend to the UV luminosity function: intrinsically the LF is approximated by a single power-law; the inclusion of dust however causes a strong break at high luminosities. Like the UV LF the line luminosity function evolves strongly with redshift, increasing by a factor ≈ 1000 from $z = 13 \rightarrow 8$.

Line EWs all increase to higher redshift, however their dependence on stellar mass is more complex due to the correlation of stellar mass with metallicity (§2.1.1) and the

Figure 1. The mass-weighted average age (top) and average metallicity of star particles with ages < 10 Myr (bottom) as a function of stellar mass for $z \in \{8, 9, 10, 11, 12, 13\}$. The solid lines show the median age/metallicity in 0.1 dex wide $\log_{10}(M_\star/M_\odot)$ bins. The 2D histogram shows the distribution of stellar masses and mean ages/metallicities at $z = 8$ using a logarithmic scale.

$z = 8$ far-UV luminosity function. For a full description see Wilkins et al. (2017).

This simple model for the reprocessing of light by gas and dust effectively assumes that ionising photons produced by star particles are immediately reprocessed by the gas. For a given star particle this means the stellar and nebular emission are equally affected by dust, leaving line equivalent
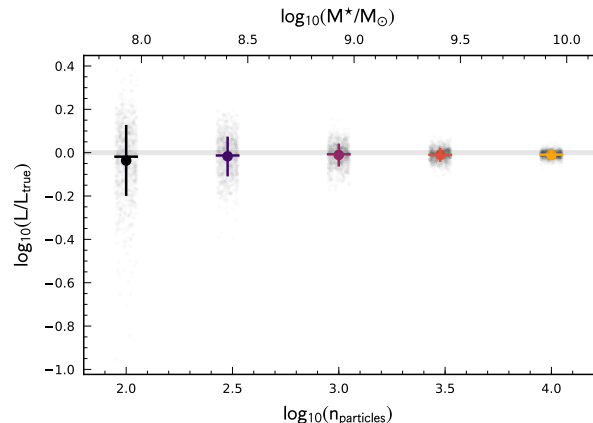
---

[2] While true for a single star particle, this is not necessarily true for an entire galaxy. For example, if star particles associated with strong nebular emission are more heavily attenuated than others the equivalent width of a line can be suppressed.
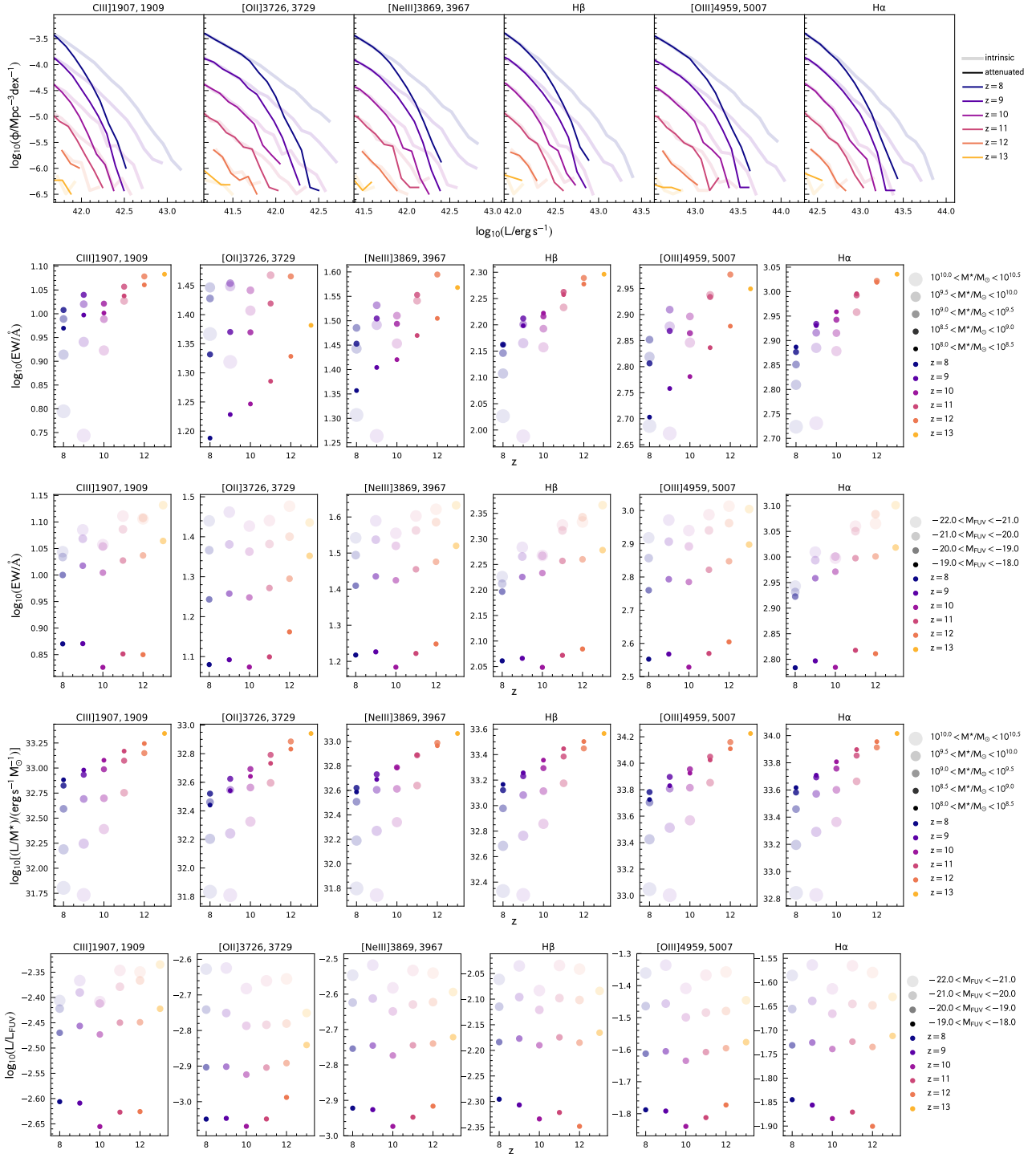
Figure 3. Predictions for the properties of 6 prominent UV and optical lines in BLUETIDES. In the top panel we show both the intrinsic and dust-attenuated luminosity functions for each line at $z \in \{8, 9, 10, 11, 12, 13\}$. In the next two rows we show the median attenuated equivalent width in bins of stellar mass and UV luminosity respectively. In the fourth row we show the median specific line luminosity ($L/M_\star$) in stellar mass bins while in the final row we show the median ratio of the line luminosity to the UV luminosity in bins of UV luminosity.

sensitivity of individual line luminosities to the metallicity (§A2.1). For example the EW of the hydrogen recombination lines drops at higher stellar mass will that of the [OII]3726, 3729 line peaks at $M^\star \sim 10^{9.5}\,\mathrm{M}_\odot$ (at $z = 8$).

3.2 Line Emission as a Tracer of Star Formation

As the LyC photon production drops off dramatically at ages $> 10\,\mathrm{Myr}$, hydrogen recombination line luminosities are often held as a gold standard of star formation activity trac-
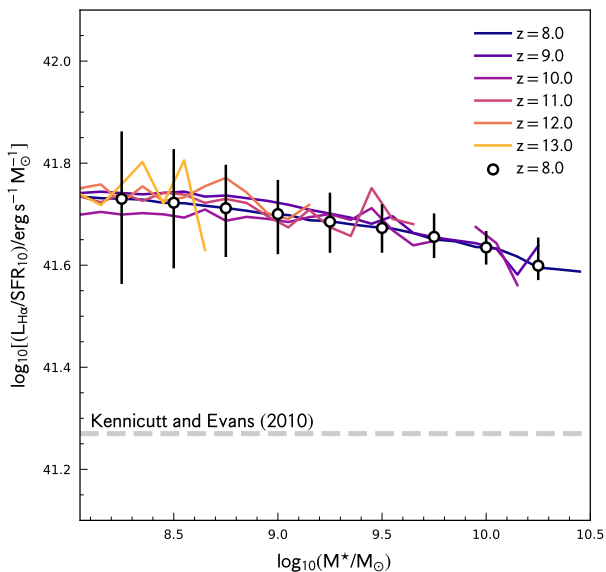
Figure 4. The ratio of the intrinsic Hα line luminosity to the recent star formation activity (the total mass in stars formed in the last 10 Myr) as a function of stellar mass. The horizontal line denotes the value suggested by Kennicutt & Evans (2012).

ers (Kennicutt & Evans 2012). In Fig. 4 we compare the intrinsic Hα luminosity to the recent ($\leq 10\,$Myr) star formation activity as a function of stellar mass and redshift. At high-masses, where star formation history sampling effects (see §2.2.1) are negligible the scatter in the ratio is very small $\log_{10}[(L_{H\alpha}/\text{SFR})/\text{erg s}^{-1}\,\text{M}_\odot^{-1}\,\text{yr}] \approx 0.05$ confirming the tight relation between line luminosity and star formation activity. There is also a slight decline with increasing stellar mass attributable to an increase in the stellar metallicity (see Fig. 1) and thus the decline in the LyC photon production rate (see Fig. A1). The increase in the scatter at low stellar masses can be attributed to the sampling effects discussed in §2.2.1.

However, the calibration inferred from this analysis is significantly different ($\approx 0.45\,$dex higher) from the value proposed by Kennicutt & Evans (2012). This reflects both the fact that the BPASS models produce more LyC photons and that the metallicity implicit in the Kennicutt & Evans (2012) calibration is higher than predicted by BlueTides.

3.3 The effect of the choice of IMF and SPS model

We must consider the effect of changing the choice of stellar population synthesis model and/or initial mass function on the luminosities and equivalent widths. However, these changes are only made at the post-processing stage and are thus not self-consistent. For example, self-consistently adopting an alternative IMF would significantly affect the production of metals which would also impact line ratios and luminosities. A summary of these changes, relative to our default choices, are shown in Fig. 5. This reveals:

• Reducing the upper-mass cut-off of the IMF from $300\,\text{M}_\text{odot}$ causes a decrease in the line luminosity of ≈ 0.15 dex while equivalent widths decrease by a smaller amount (≈ 0.1 dex) as the continuum is also reduced.

• Flattening the slope ($\alpha_2 = 2.35 \rightarrow 2.0$) increases the number of high-mass stars per unit stellar mass increasing the number of LyC photons and thus causing an increase in line luminosities (≈ 0.45). Equivalent widths are also increased, but by a smaller amount ($\approx 0.1 - 0.2$) with the amount sensitive to the line and redshift. The redshift evolution arises because at higher redshift the continuum is increasingly dominated by the most massive stars. It is also important to note that flattening the IMF in this way would also increase the far-UV continuum luminosities of galaxies breaking the otherwise good agreement with observations (see Wilkins et al. 2017). This could be ameliorated by having more agressive dust attenuation.

• The effect of steepening the slope ($\alpha_2 = 2.35 \rightarrow 2.7$) produces the opposite effect, though with a slightly different magnitude: line luminosities decrease by ≈ 0.6 dex while equivalent widths decrease by $\approx 0.15 - 0.25$ dex. Steepening the IMF to this extent will also significantly decrease the far-UV continuum luminosities again breaking the good agreement with observational constraints. In this case the good agreement can not be recovered without more drastic changes to the simulation physics.

• Adopting previous generations (2.2 or 2.1) of the BPASS models produces only relatively small changes (< 0.1 dex) to the predicted line luminosities and equivalent widths.

• Adopting the Pegase.2 SPS model (and $m_\text{up} = 100\,\text{M}_\text{odot}$) produces a significant decrease in the luminosities and equivalent widths relative to our default model. For most lines luminosities drop by ~ 0.5 dex while equivalent widths drop by ~ 0.3. While some of this decrease can be attributed to the small upper-mass cutoff of the IMF most of the effect is attributed to wider modelling differences between Pegase.2 and BPASS.

3.4 Comparison with existing observational constraints

As noted in the introduction there remain few constraints (direct or otherwise) on line emission at very high-redshift.

3.4.1 Direct

The majority of direct constraints come from observations of Lyman-α (). However, the Lyman-α line is resonantly scattered by the ISM/IGM significantly complicating its modelling. For this reason we have omitted a detailed comparison with Lyman-α observations. We do however nevertheless make predictions for the intrinsic Lyman-α properties, where intrinsic in this context includes dust attenuation but not scattering by the ISM/IGM. These predictions are presented in Appendix B.

Recently Stark et al. (2015a) and Stark et al. (2017) have obtained constraints on the [CIII],CIII] at $z = 6 - 8$. These constraints are shown in Fig. 6 alongside predictions from BlueTides. These constraints are broadly in line BlueTides predictions with the exception of EGS-z8-1
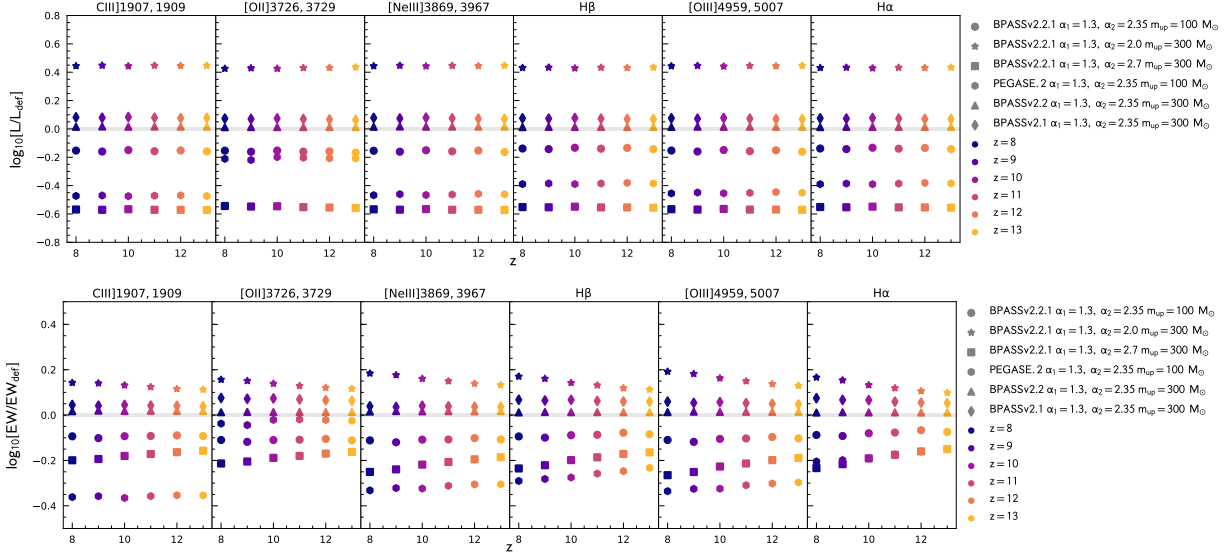
Figure 5. The effect of changing the choice of stellar population synthesis model and/or initial mass function on the luminosities and equivalent widths of the 6 lines relative to our default choices (BPASSv2.2.1, $\alpha_2 = 2.35$, $m_{up} = 300\,M_\odot$).
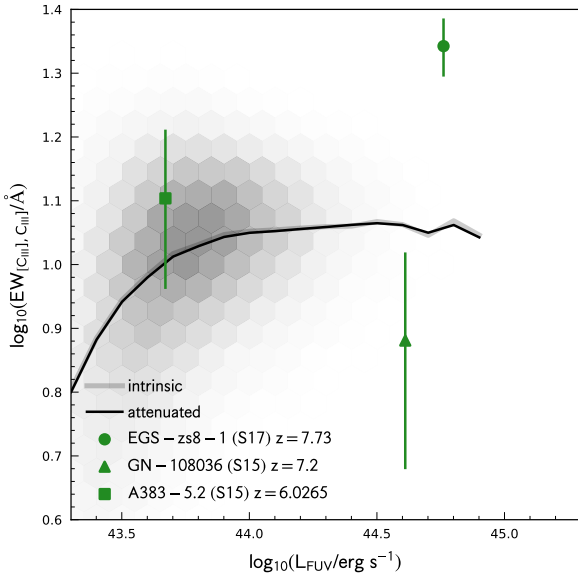

Figure 6. The predicted distribution of [CIII],CIII equivalent width and observed far-UV luminosity at $z \sim 8$. Points denote individual objects from $z = 5 - 8$.

(Stark et al. 2017) which has a measured EW ~ 0.3 dex above the predictions. However, it is important to note that our predictions do not include an AGN component which may explain the high EW observed in EGS-z8-1 (Nakajima et al. 2018).

3.4.2   Indirect

Indirect constraints on the strength of the strongest optical lines are possible through the effect of these lines on
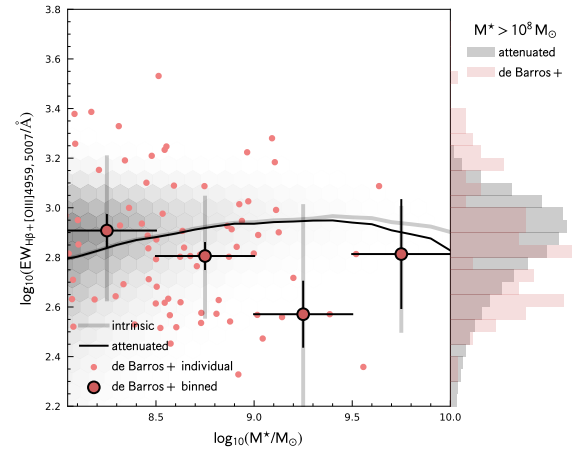
Figure 7. The observed deBarros (2019) and predicted distribution of combined Hβ and [OIII]λ4959,5007 equivalent widths and stellar masses at $z \sim 8$. The small red circles show the individual measurements from deBarros (2019) while the large point denote the median value in 0.5 dex wide bins of stellar mass. The small and large error bars denote the error on the median and the 16-84th percentile range respectively. The dark and light solid lines show the intrinsic and attenuated predictions from BLUETIDES respectively. The histograms on the right hand side show the distribution of equivalent widths for galaxies with $M^\star > 10^8\,M_\odot$.

broad-band photometry (e.g. Schaerer & de Barros 2010; Stark et al. 2013; Wilkins et al. 2013; Smit et al. 2014; Wilkins et al. 2016a; deBarros 2019). deBarros (2019) recently combined *Hubble* and *Spitzer* observations probing the rest-frame UV and optical to constrain the prominent Hβ and [OIII]λ4959,5007 lines at $z \approx 8$. As shown in Fig. 7 the Hβ + [OIII] EW distribution measured by deBarros (2019) closely overlaps with that predicted by BLUETIDES.

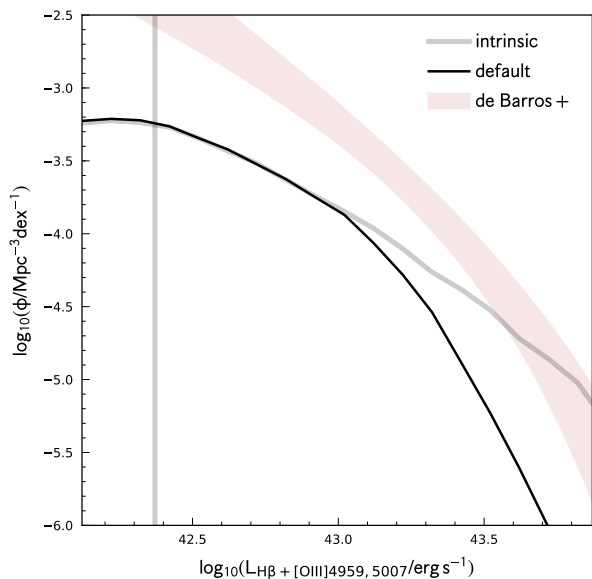**Figure 8.** The observed deBarros (2019) and predicted combined Hβ and [OIII]λ4959,5007 line luminosity function at $z \sim 8$.
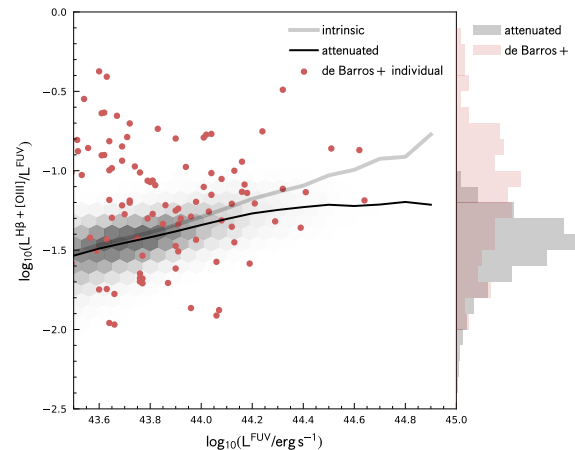

Figure 9. The observed deBarros (2019) and predicted distribution of the ratio of the Hβ and [OIII]λ4959,5007 line luminosities to the far-UV luminosity and far-UV luminosities at $z \sim 8$. The small red circles show the individual measurements from deBarros (2019). The dark and light solid lines show the intrinsic and attenuated predictions from BlueTides respectively. The histograms on the right hand side show the distribution of ratios for galaxies with $M^\star > 10^8 \, \mathrm{M}_\odot$.
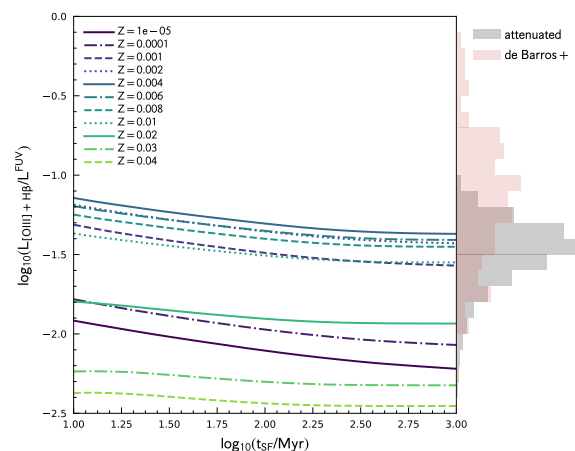
Unfortunately this good agreement is not seen in the luminosity function, as shown in Fig. 8, which is systematically offset to higher luminosities (~ 0.3 dex) or higher space densities (~ 0.7 dex). The cause of this discrepancy appears to lie in the relation between the combined line luminosity and the far-UV luminosity, which is used to convert the observed far-UV luminosity function to a line luminosity function. The individual values measured by deBarros (2019) for this are shown in 9 and are compared to the values predicted by BlueTides. The measured values appear to be on average ~ 0.3 dex higher than predicted by BlueTides. As many of the measured values are above the intrinsic expectation (see Fig. 10) one interpretation of this discrepancy is that deBarros (2019) measure higher dust attenuations than predicted by BlueTides. It is also possible that differences between the measured and predicted values of the metallicity, age, ionisation parameter, and hydrogen density can have an effect. Given the limited observational constraints such differences may not be surprising considering the range of degeneracies present.

With the arrival of the *Webb Telescope* it will be possible to obtain direct measurements of individual line luminosities and equivalent widths for a large range of galaxies at $z \sim 8$ and beyond providing a much clearer assessment of whether these predictions match the real Universe.

4 CONCLUSIONS

The *Webb Telescope* will provide the opportunity to measure the rest-frame optical emission lines of galaxies in the (EoR, $8 < z < 13$). By combining the large cosmological hydrodynamical simulation BlueTides with photoionisation modelling we have made predictions for emission line properties of galaxies with $M^\star > 10^8 \, \mathrm{M}_\odot$ in the EoR.

Figure 10. The Hβ and [OIII]λ4959,5007 line luminosities - far-UV luminosity ratio measured by deBarros (2019) compared to predictions from photoionisation modelling assuming a constant star formation activity ($t = 10 \rightarrow 1000 \, \mathrm{Myr}$) and a range of metallicities. The histograms on the right hand side show both the observed and predicted distribution of ratios for galaxies with $M^\star > 10^8 \, \mathrm{M}_\odot$.

• While the Hα luminosity is found to be strongly correlated with recent star formation activity we find a large offset ($0.3 - 0.4$ dex higher) between the Kennicutt & Evans (2012) calibration and our results. This reflects both the adoption of the BPASS stellar population synthesis models and the lower metallicity of the stellar populations.

• Bluetides matches recent indirect observational con-

straints on the Hβ + [O III]λ4959,5007 equivalent width distribution but fails to match the inferred luminosity function.

REFERENCES

Baldwin J. A., Phillips M. M., Terlevich R., 1981, Publications of the Astronomical Society of the Pacific, 93, 5

Brinchmann J., Charlot S., White S. D. M., Tremonti C., Kauffmann G., Heckman T., Brinkmann J., 2004, MNRAS, 351, 1151

Caruana J., Bunker A. J., Wilkins S. M., Stanway E. R., Lacy M., Jarvis M. J., Lorenzoni S., Hickey S., 2012, MNRAS, 427, 3055

Caruana J., Bunker A. J., Wilkins S. M., Stanway E. R., Lorenzoni S., Jarvis M. J., Ebert H., 2014, MNRAS, 443, 2831

Chabrier G., 2003, PASP, 115, 763

Di Matteo T., Croft R. A. C., Feng Y., Waters D., Wilkins S., 2016, preprint, (arXiv:1606.08871)

Feng Y., Di Matteo T., Croft R., Tenneti A., Bird S., Battaglia N., Wilkins S., 2015, ApJ, 808, L17

Feng Y., Di-Matteo T., Croft R. A., Bird S., Battaglia N., Wilkins S., 2016, MNRAS, 455, 2778

Ferland G. J., et al., 2017, Rev. Mex. Astron. Astrofis., 53, 385

Finkelstein S. L., et al., 2013, Nature, 502, 524

Hinshaw G., et al., 2013, ApJS, 208, 19

Kennicutt R. C., Evans N. J., 2012, ARA&A, 50, 531

Nakajima K., et al., 2018, A&A, 612, A94

Pentericci L., et al., 2011, ApJ, 743, 132

Reddy N. A., et al., 2015, ApJ, 806, 259

Schaerer D., de Barros S., 2010, A&A, 515, A73

Shapley A. E., Steidel C. C., Pettini M., Adelberger K. L., 2003, ApJ, 588, 65

Smit R., et al., 2014, ApJ, 784, 58

Stark D. P., Ellis R. S., Chiu K., Ouchi M., Bunker A., 2010, MNRAS, 408, 1628

Stark D. P., Ellis R. S., Ouchi M., 2011, ApJ, 728, L2

Stark D. P., Schenker M. A., Ellis R., Robertson B., McLure R., Dunlop J., 2013, ApJ, 763, 129

Stark D. P., et al., 2015a, MNRAS, 450, 1846

Stark D. P., et al., 2015b, MNRAS, 454, 1393

Stark D. P., et al., 2017, MNRAS, 464, 469

Steidel C. C., Giavalisco M., Pettini M., Dickinson M., Adelberger K. L., 1996, ApJ, 462, L17

Tremonti C. A., et al., 2004, ApJ, 613, 898

Waters D., Di Matteo T., Feng Y., Wilkins S. M., Croft R. A. C., 2016b, preprint, (arXiv:1605.05670)

Waters D., Wilkins S., Di Matteo T., Feng Y., Croft R., Nagai D., 2016a, preprint, (arXiv:1604.00413)

Wilkins S. M., et al., 2013, MNRAS, 435, 2885

Wilkins S. M., Feng Y., Di-Matteo T., Croft R., Stanway E. R., Bunker A., Waters D., Lovell C., 2016a, preprint, (arXiv:1605.05044)

Wilkins S. M., Feng Y., Di-Matteo T., Croft R., Stanway E. R., Bouwens R. J., Thomas P., 2016b, MNRAS, 458, L6

Wilkins S. M., Feng Y., Di-Matteo T., Croft R., Lovell C. C., Waters D., 2017, preprint, (arXiv:1704.00954)

deBarros S., 2019, 336, 25
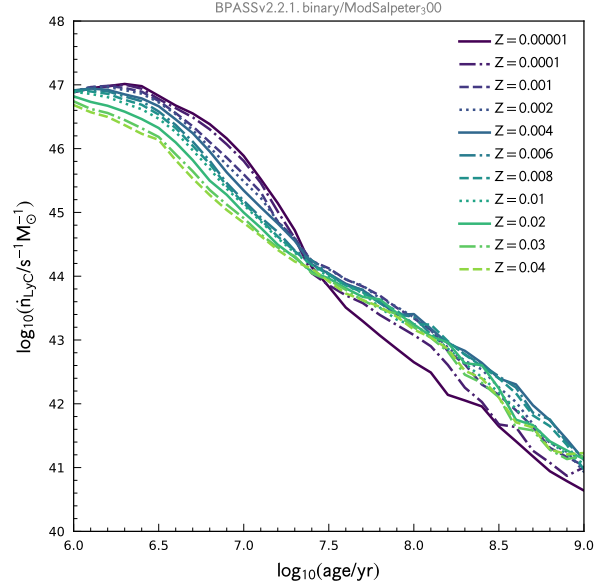

The production rate of Lyman continuum (LyC) photons (H I ionising) produced by a simple stellar population (SSP) per unit initial mass as a function of age for a range of different metallicities.

APPENDIX A: PHOTOIONISATION MODELLING

To predict the emission line properties of galaxies in the BlueTides simulation we assume that each star particle forms its own H II region based on its age and metallicity.

Because each star particle is modelled as a simple (with a single age and metallicity) stellar population (SSP) it is useful to (in §A1) explore how the rate of Lyman continuum (LyC) photon production, and the hardness of the ionising photon continuum, is affected by the age, metallicity, initial mass function (IMF), and choice of stellar population synthesis (SPS) model. In §A2 we then describe our photoionisation modelling procedure and explore how various lines are sensitive to parameters such as the gas/stellar metallicity, ionisation parameter, and hydrogen density.

A1   The Production of Ionising Photons

The LyC production rate of a SSP depends on both its age and metallicity. This is demonstrated in Fig. A1, where we show the LyC production rate $\dot{n}_{\rm LyC}$ as a function of age for a range of different metallicities assuming the BPASS model and a modified Salpeter IMF extending to $300\,{\rm M}_\odot$. The production rate drops rapidly after the first few million years at higher ages and metallicities, declining by $\sim 10-100$ as the population ages from $1 \rightarrow 10\,{\rm Myr}$ and then again by a factor of ~ 100 from $t = 10 \rightarrow 100\,{\rm Myr}$. At young ages ($< 20\,{\rm Myr}$) the lowest metallicity populations can produce up-to 10 times as many LyC photons, though at later times this trend reverses.

The overall difference in the production of LyC photons as a function of metallicity is summarised in Fig. A2 where
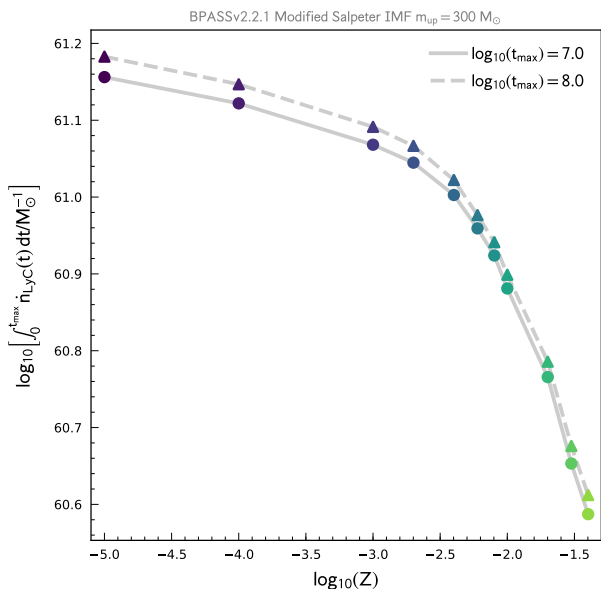
Figure A2. The total number of LyC photons produced by SSP over the first 10 and 100 Myr as a function of metallicity.

we show the *total* number of LyC photons produced by an SSP from $t = 0 \rightarrow 10^7$ yr and $t = 0 \rightarrow 10^8$ yr. The lowest metallicity modelled ($Z = 10^{-5}$) SSP considered produces approximately double the number LyC photons over its lifetime compared to $Z = 0.01$.

A1.1 The Ionising Photon Hardness

More complex atoms have a range of potential ionisation states each excited by photons of different energies. For example, Helium can be singly ionised by photons with $E_\gamma > 24.6\,\mathrm{eV}$ and doubly ionised by those with $E_\gamma > 54.4\,\mathrm{eV}$. For this reason it is useful to also consider the ionising photon hardness, essentially a ratio of the number of more energetic photons to $\dot{n}_{\mathrm{LyC}}$. The left panel of Fig. A3 shows the hardness the LyC by comparing the number of LyC and OII ($> 35.1\,\mathrm{eV}$) energy photons as a function of age for two metallicities $Z \in \{0.02, 0.004\}$. At the youngest ages the higher metallicity SSP produces significantly fewer (~ 1 dex) harder photons. For older ($> 10\,\mathrm{Myr}$) populations the hardness is similar.

A1.2 The Choice of Initial Mass Function and SPS Model

It is crucial to note that both the number of LyC photons and the shape of the ionising spectrum predicted for a given SSP is sensitive to the a range of stellar evolution and atmosphere modelling assumptions and thus choice of stellar population synthesis (SPS) model (see also **??**). The middle panel of Fig. A3 shows a comparison between $\dot{n}_{\mathrm{LyC}}$ for different SPS models/versions; these include the three most recent versions of BPASS (v2.2.1, v2.2, v2.1) and the PEGASE.2 model (**?**). This analysis reveals relatively small differences between the different BPASS versions but larger differences between BPASS and PEGASE.2. This difference is particularly

acute at ages $> 5\,\mathrm{Myr}$ where the LyC production rate predicted by PEGASE.2 drops of much more rapidly than in BPASS. The left panel of Fig. A3 shows the difference in the hardness between the default model and BPASS; again, the most notable feature is the difference at $> 5\,\mathrm{Myr}$.

Both the production rate and hardness are also affected by the choice of initial mass function (IMF). The right hand panel of Fig. A3 shows the production rate relative to our default model for several different high-mass slopes $\alpha \in \{2.0, 2.35, 2.7\}$ and for a lower ($100\,\mathrm{M}_\odot$) high-mass cut-off. Assuming a shallower slope ($\alpha = 2.0$) yields more around double the number of LyC photons overall with the enhancement decreasing with age. Assuming a steeper slope has the opposite effect albeit with a slightly larger magnitude. Adopting a lower high-mass cut-off reduces the number of LyC photons produced at the youngest ages, overall leading to around $\sim 30 - 50\%$ less LyC photons produced by the SSP over its lifetime, depending on the metallicity.

A2 Photoionisation Modelling

We now turn our attention to modelling the nebular continuum and line emission associated with a SSP. To do so we take advantage of the 2017 (C17.01) version of the popular CLOUDY code (Ferland et al. 2017)[3].

To model the nebular emission associated with a stellar population we adopt a similar approach to **?** (see also **??**). Like these works we choose characterise our photoionisation modelling using the density of hydrogen (n_H) and ionisation parameter at the Stromgren radius U_S. This is defined as,

$$U_S \propto \left(Q\epsilon^2 n_H\right)^{1/3} \tag{A1}$$

where ϵ is the effective gas filling factor.

We differ from previous approaches by parameterising models for the ionising spectrum in terms of an ionisation parameter defined at a reference age ($t = 1\,\mathrm{Myr}$) and metallicity ($Z = 0.02$) - $U_{S,\mathrm{ref}}$. Because of this the actual ionisation parameter passed to CLOUDY depends on the ionising photon production rate relative to the reference value, i.e.

$$U_S = U_{S,\mathrm{ref}} \left(\frac{Q}{Q_{\mathrm{ref}}}\right)^{1/3}. \tag{A2}$$

This ensures that the assumed geometry of the HII region, encoded in the $\epsilon^2 n_H$ term, is fixed for different metallicities/ages. By default we assume $\log_{10}(U_{S,\mathrm{ref}}) = -2$ and $\log_{10}(n_H/\mathrm{cm}^{-3}) = 2.5$.

We further assume that the metallicity of the HII region is the same as the stellar population and adopt the same interstellar abundances and dust depletion factors as **?**. It is however worth noting that the detailed elemental abundances assumed as a function of metallicity differ between that assumed in stellar population synthesis models and what we assume for the ISM.

A2.1 Line Luminosities and Equivalent Widths

Using the modelling procedure described above we now make predictions for line luminosity and equivalent widths. We
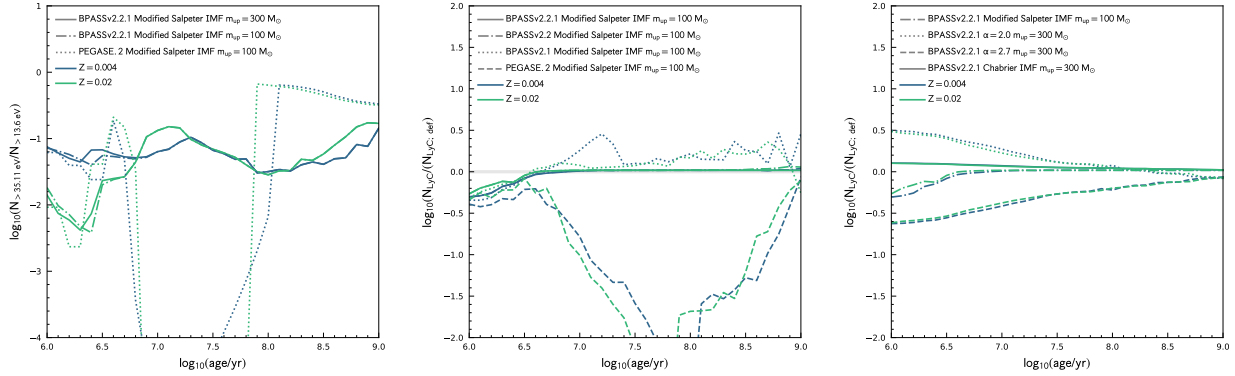
---

[3] https://www.nublado.org

Figure A3. *Left:* The hardness of the ionising of photon spectrum (defined as the ratio of to HI ionising photons) as a function of age for two metallicities and three SPS model / IMF combinations. *Centre:* The difference between the number of LyC photons produced assuming alternative SPS models. *Right:* The difference between the number of LyC photons produced assuming alternative initial mass functions.

concentrate here on 12 prominent UV and optical lines. In making these predictions we assume a constant star formation history with fixed metallicity.

Fig. A4 shows the predicted line luminosities (per unit stellar mass) and equivalent widths (EWs) for a range of prominent rest-frame UV and optical emission lines as a function of metallicity. In both cases we assume continuous star formation for 10 Myr. The luminosity of the hydrogen lines largely track the change in the LyC production rate with metallicity with the luminosity dropping by ~ 0.5 dex over the metallicity range considered. The non-hydrogen lines exhibit more complicated behaviour with an increase to $Z \sim 10^{-2.5}$ before declining to higher metallicities. The rapid increase broadly reflects the increasing abundance of each element in the ISM while the drop at high metallicities reflects the decline in the number of suitably energetic photons. The metallicity dependence of the EW of each line exhibits a similar behaviour, albeit often with reduced magnitude.

The equivalent width of any line is also sensitive the star formation history of the stellar population. Fig. A5 shows how the equivalent width of Hα varies with the duration of continuous star formation for a range of metallicities. The equivalent width declines from $\sim 1000 - 2000$ after to 10 Myr to $\sim 150 - 300$ after 1 Gyr.

A2.2 The Effect of Photoionisation Modelling Assumptions

The luminosity and EW width of each line is also sensitive to additional modelling assumptions including the choice of SPS model, IMF, but also the parameters encapsulating the geometry, density, and excitation of the H II region. As noted above we parameterise these in terms of the ionisation parameter, which effectively encodes the geometry of the region, and the hydrogen density.

Fig. A6 demonstrates the effect on changing both the reference ionisation parameter $U_{S,\mathrm{ref}}$ and hydrogen density n_H on the strengths of the same 12 prominent lines considered previously. **Expand**

APPENDIX B: DETAILED PREDICTIONS FOR INDIVIDUAL LINES

In Figs. B1-B4 we show the EW and luminosity as a function of stellar mass and observed UV luminosity for each line in addition to the luminosity function. Need a table with all this in.
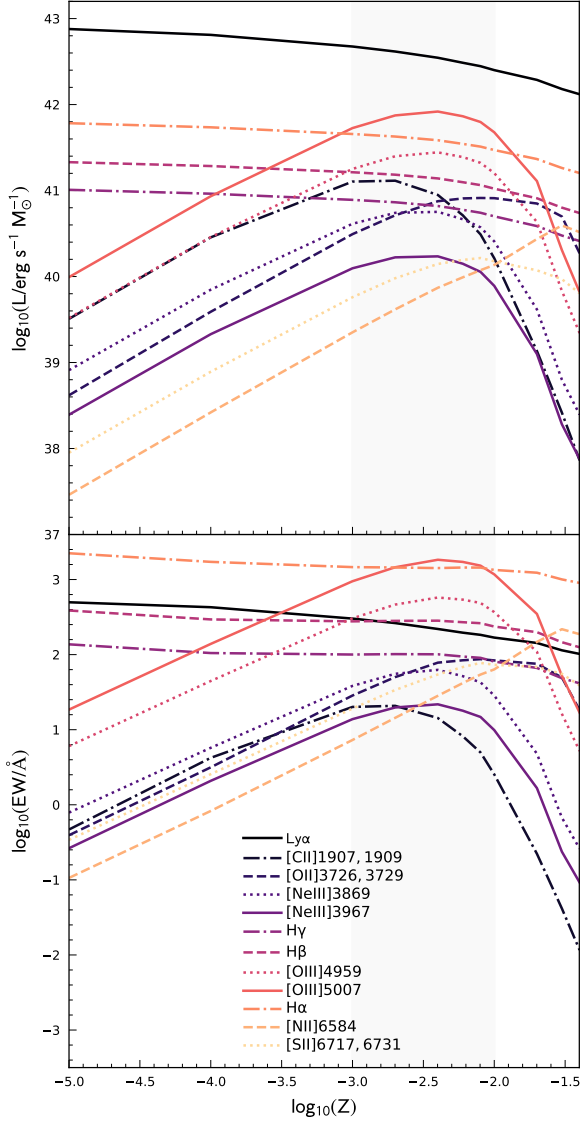
Figure A4. The predicted intrinsic luminosity (top) and equivalent width (bottom) as a function of metallicity for a range of prominent emission lines in the rest-frame UV and optical. In both cases we assume constant star formation for 10 Myr. The thick grey band denotes the rough range of metallicities predicted by BlueTides for galaxies with $M^* > 10^8 \, M_\odot$.
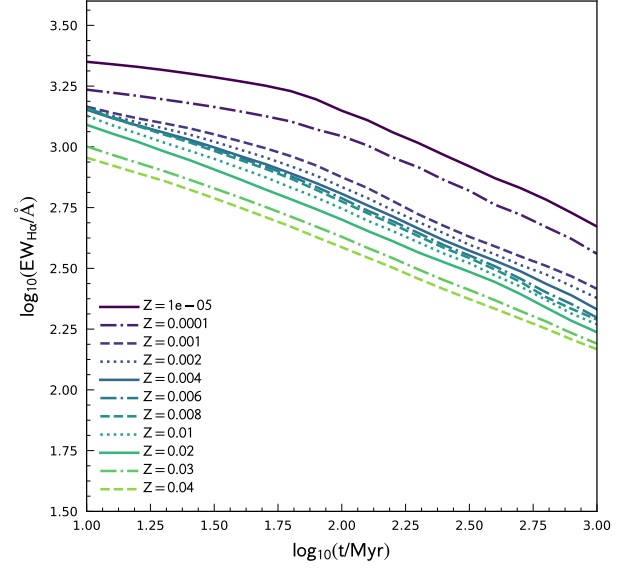

Figure A5. The evolution of the Hα equivalent width assuming continuous star formation for a range of metallicities.
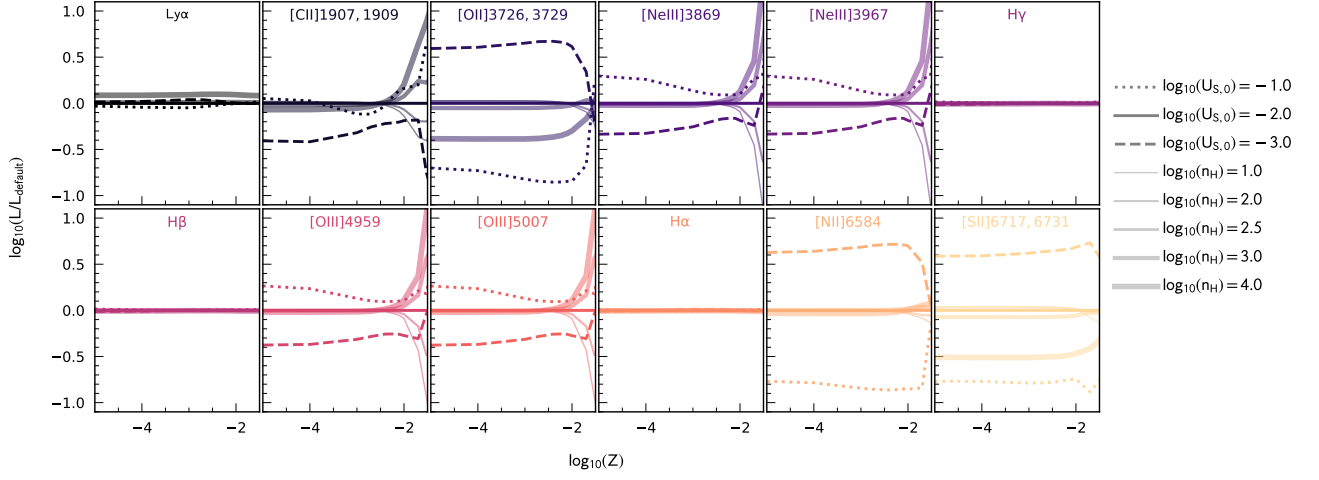
Figure A6. The effect of changing the ionisation parameter $U_{S,\mathrm{ref}}$ and hydrogen density n_H of the relative luminosity of each of the emission lines considered in this work. The default model assumes $\log_{10}(U_{S,\mathrm{ref}}) = -2$ and $\log_{10}(n_H/cm^{-3}) = 2.5$.
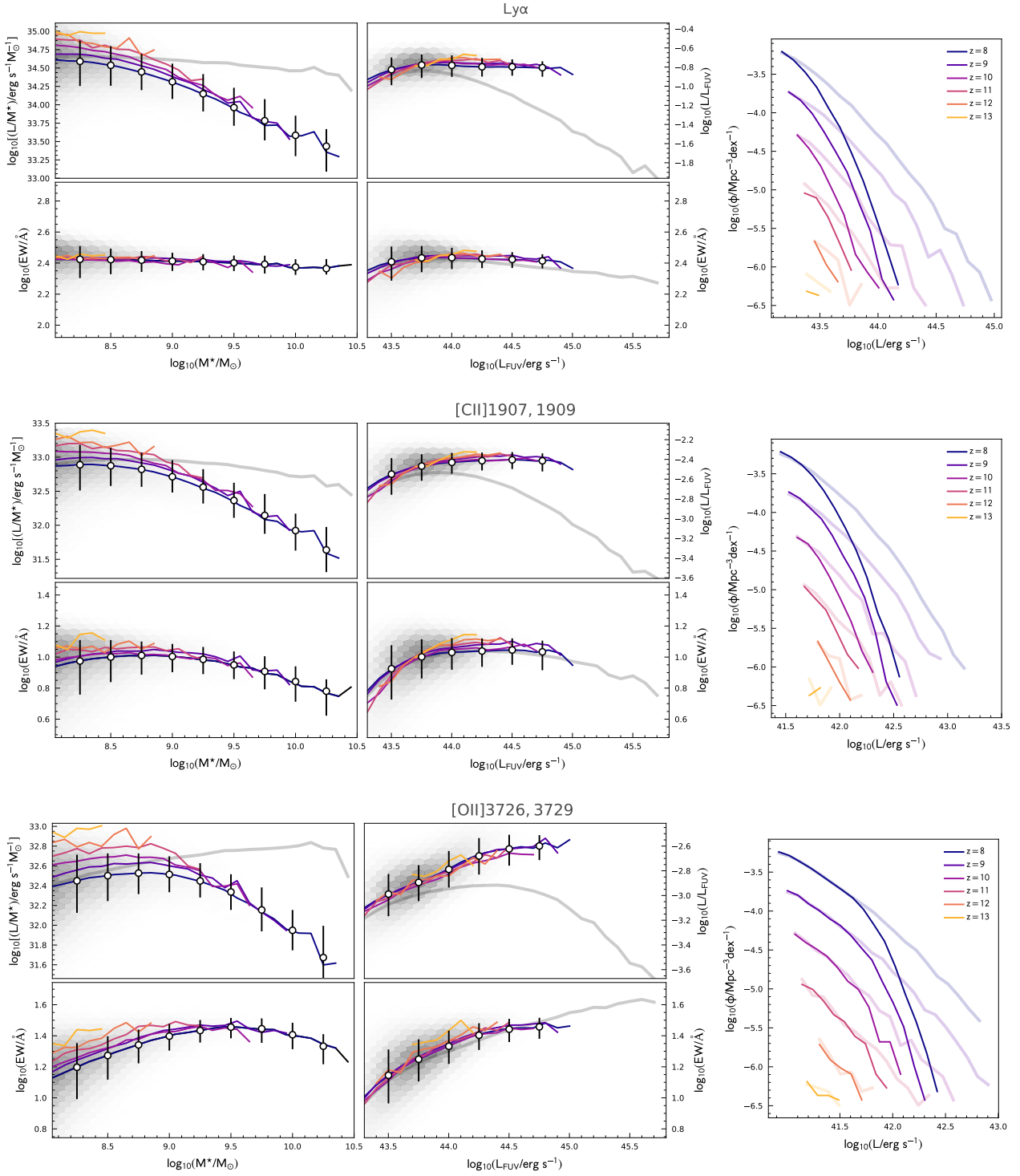
Figure B1. I could not, would not, on a boat. I will not, will not, with a goat. I will not eat them in the rain. I will not eat them on a train. Not in the dark! Not in a tree! Not in a car! You let me be! I do not like them in a box. I do not like them with a fox. I will not eat them in a house. I do not like them with a mouse. I do not like them here or there. I do not like them ANYWHERE! I do not like green eggs and ham! I do not like them, Sam-I-am.
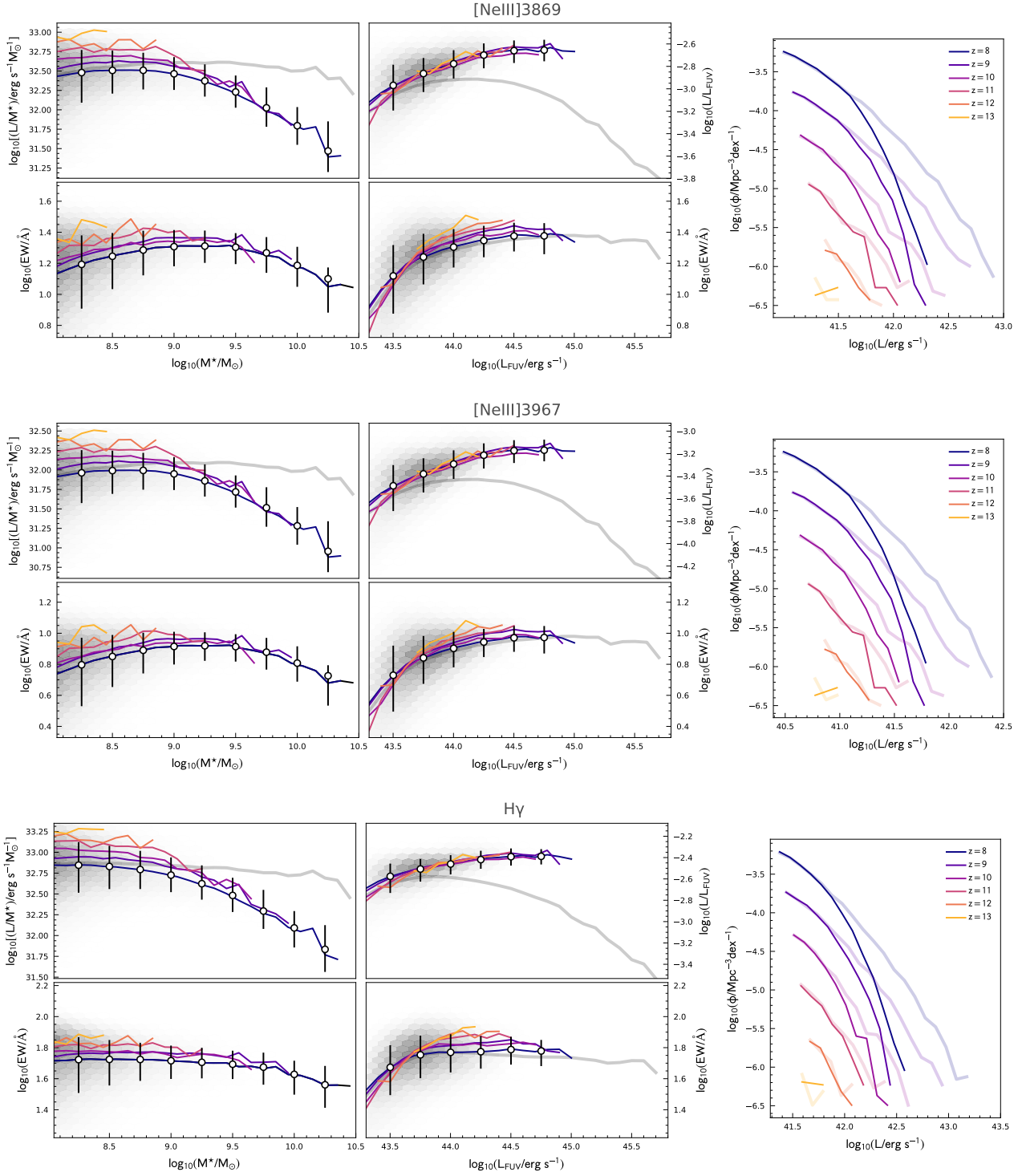
Figure B2. I could not, would not, on a boat. I will not, will not, with a goat. I will not eat them in the rain. I will not eat them on a train. Not in the dark! Not in a tree! Not in a car! You let me be! I do not like them in a box. I do not like them with a fox. I will not eat them in a house. I do not like them with a mouse. I do not like them here or there. I do not like them ANYWHERE! I do not like green eggs and ham! I do not like them, Sam-I-am.
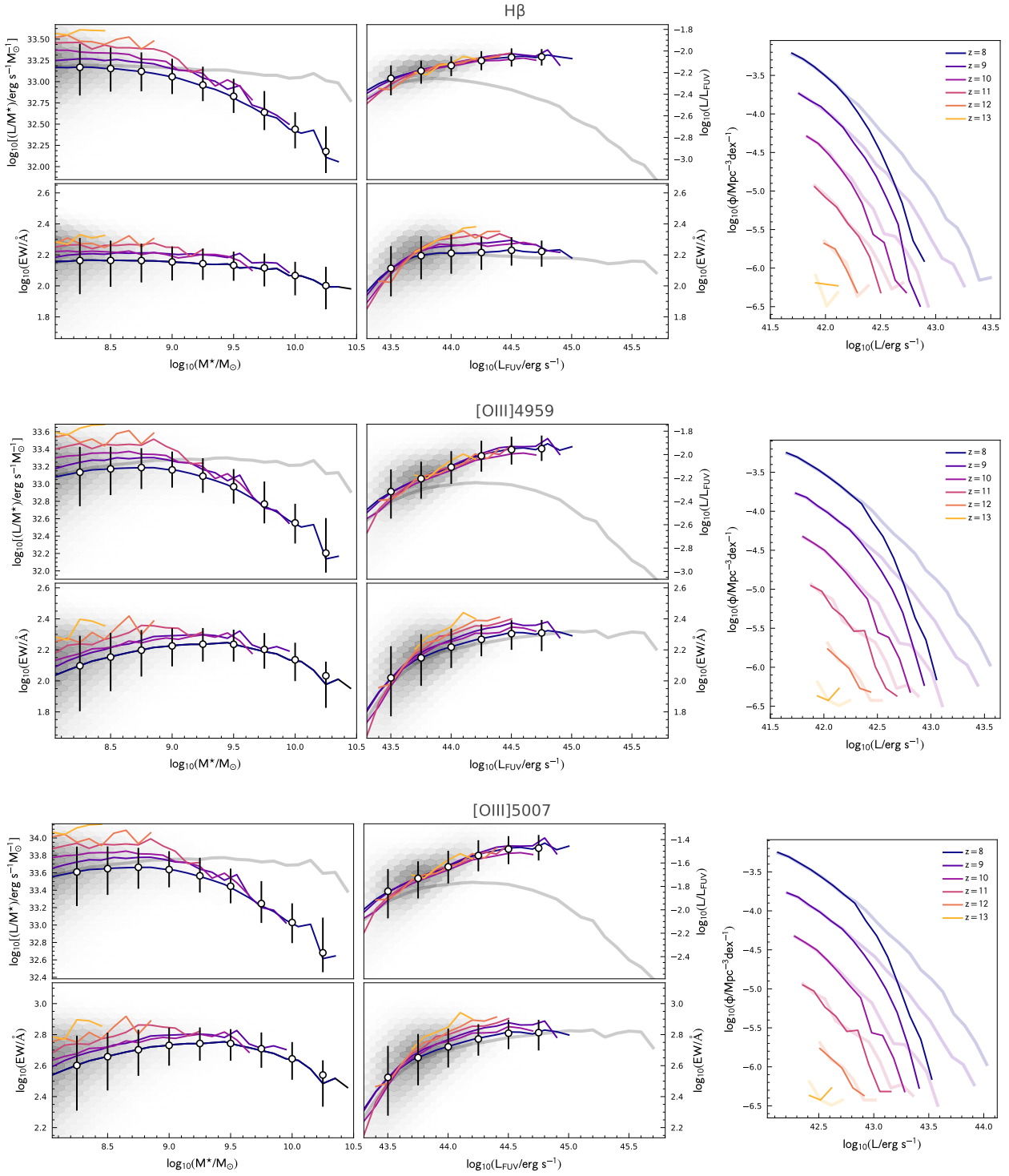
Figure B3. I could not, would not, on a boat. I will not, will not, with a goat. I will not eat them in the rain. I will not eat them on a train. Not in the dark! Not in a tree! Not in a car! You let me be! I do not like them in a box. I do not like them with a fox. I will not eat them in a house. I do not like them with a mouse. I do not like them here or there. I do not like them ANYWHERE! I do not like green eggs and ham! I do not like them, Sam-I-am.
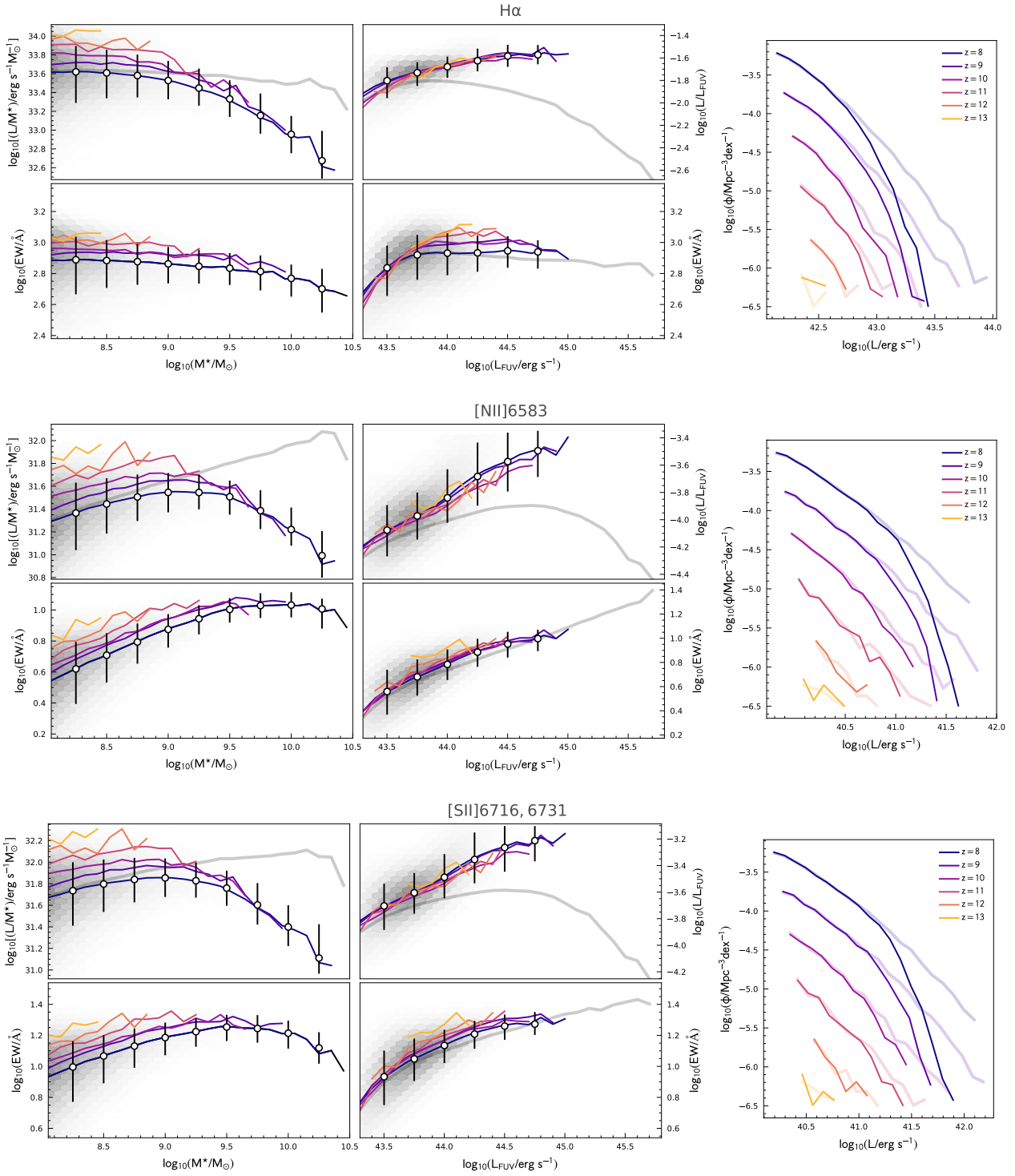
Figure B4. I could not, would not, on a boat. I will not, will not, with a goat. I will not eat them in the rain. I will not eat them on a train. Not in the dark! Not in a tree! Not in a car! You let me be! I do not like them in a box. I do not like them with a fox. I will not eat them in a house. I do not like them with a mouse. I do not like them here or there. I do not like them ANYWHERE! I do not like green eggs and ham! I do not like them, Sam-I-am.